This article has been accepted for inclusion in a future issue of this journal. Content is final as presented, with the exception of pagination.

A Deep Learning Approach for Microwave and Millimeter-Wave Radiometer Calibration

Mehmet Ogut, Xavier Bosch-Lluis, and Steven C. Reising, *Senior Member, IEEE*

***Abstract*— Deep learning artificial neural network techniques can be applied for on-orbit calibration of microwave and millimeter-wave radiometer spaceborne instruments, including those for small satellites. The noise-wave model has been employed for noise characterization and validation of the proposed deep learning calibration technique for a synthetically generated Dicke-switching radiometer. The developed deep learning neural network radiometer calibrator produces high accuracy estimates of antenna temperatures from the measurements of radiometer output voltage and thermistor readings. Tests with noise-free and noisy samples of the developed model have shown that the proposed calibration method does not add any significant noise to the radiometer calibration. The performance of the proposed method does not degrade with increased nonlinearity for a radiometer, while nonlinearity is a challenging issue for conventional calibration techniques. The deep learning calibration model learns the radiometer noise characteristics from radiometer prelaunch measurements during thermal vacuum chamber testing. The neural network calibrator proposed in this paper has self-learning capability during the on-orbit operation of a radiometer that can be used to improve the performance of on-orbit calibration. The proposed technique is demonstrated by comparing the residual uncertainty of the deep learning calibration with the theoretical value. No numerical study is presented to compare the performance with conventional calibration techniques. The new method may be solely applied to calibrate the radiometer or applied along with conventional calibration techniques.**

***Index Terms*— Calibration, CubeSats, deep learning, microwave radiometer, millimeter-wave radiometer, neural network, noise-wave model.**

I. Introduction

Microwave and millimeter-wave radiometers have been widely used to improve understanding of the distribution of atmospheric water vapor and its dynamics for decades to provide information for studies in hydrology, agriculture, meteorology, climatology, and oceanography [1], [2]. Accuracy, sensitivity, stability, and measurement uncertainty are used as figures of merit of a radiometer. The accuracy of a radiometer determines the reliability of the retrieved parameters from the measurements. On the other hand, radiometric resolution (sometimes called sensitivity) provides the minimum detectable change of a radiometer due to its internal noise. Therefore, improved accuracy and radiometric resolution improve the quality of the geophysical products retrieved from radiometric measurements, including water vapor, cloud water and ice contents, soil moisture, sea-surface wind speed, and superficial sea salinity [3].

Calibration plays a major role in determining the radiometric accuracy and stability. Microwave and millimeter-wave radiometers are usually calibrated using a two-point calibration scheme by measuring two external calibration targets at widely separated, known temperatures [4]. Assuming a linear response of the radiometer without gain fluctuations, the radiometric calibration of output voltage to antenna temperature can be performed using end-to-end calibration. However, the radiometer gain fluctuates due to inherent instabilities in the radiometer's amplifiers and electronics. To account for these fluctuations and to improve the stability, radiometer architectures were developed to use internal calibration techniques, such as noise diodes for noise injection radiometers and reference loads for Dicke-switching radiometers [5].

Radiometers have been used to perform passive remote sensing of earth resources and environment from ground-based [6], airborne [7]–[9], and satellite platforms [10], [11] since the 1970s. During the past few years, interest has greatly increased in earth remote sensing from small satellites (SmallSats), especially CubeSats [12]. The CubeSat standard is based on a Unit (1U) with the volume of a 10-cm cube and a mass of up to 1.33 kg [13]. The mass and volume of a multiple-unit CubeSat ranging up to at least 12U is scaled with reference to 1U, with recent standards allowing 50% greater mass density for 6U than for 3U [14]. Advances in attitude determination and control systems, computing and communication technology, and developments in integrated circuit design and manufacturing technology have substantially reduced satellites into a small form factor. In addition, CubeSats have much a lower cost of design, launch, and operation than traditional larger satellites. For these reasons, an increasing number of microwave and millimeter-wave radiometers is being deployed on CubeSat missions. Among them, the Temporal Experiment for Storms and Tropical Systems—Demonstration (TEMPEST-D) CubeSat mission is led by Colorado State University (CSU) in partnership with the NASA Jet Propulsion Laboratory and Blue Canyon Technologies. TEMPEST-D is a 6U CubeSat mission deploying new satellite technology

Manuscript received May 14, 2018; revised September 17, 2018, January 13, 2019, and February 1, 2019; accepted February 1, 2019. This work was supported in part by the U.S. National Aeronautics and Space Administration, Science Mission Directorate, in part by the Earth Science Division Technology Office, as part of the Instrument Incubator Program under Grant NNX14AK70G, and in part by the Earth Science Division Flight Venture Program under Grant NNX15AP56G. *(Corresponding author: Mehmet Ogut.)*

M. Ogut and X. Bosch-Lluis were with the Microwave Systems Laboratory, Colorado State University, Fort Collins, CO 80523, USA. They are now with the Jet Propulsion Laboratory, California Institute of Technology, Pasadena, CA 91109, USA (e-mail: mehmet.ogut@jpl.nasa.gov).

S. C. Reising is with the Microwave Systems Laboratory, Colorado State University, Fort Collins, CO 80523, USA (e-mail: steven.reising@colostate.edu).

Color versions of one or more of the figures in this paper are available online at http://ieeexplore.ieee.org.

Digital Object Identifier 10.1109/TGRS.2019.2899110

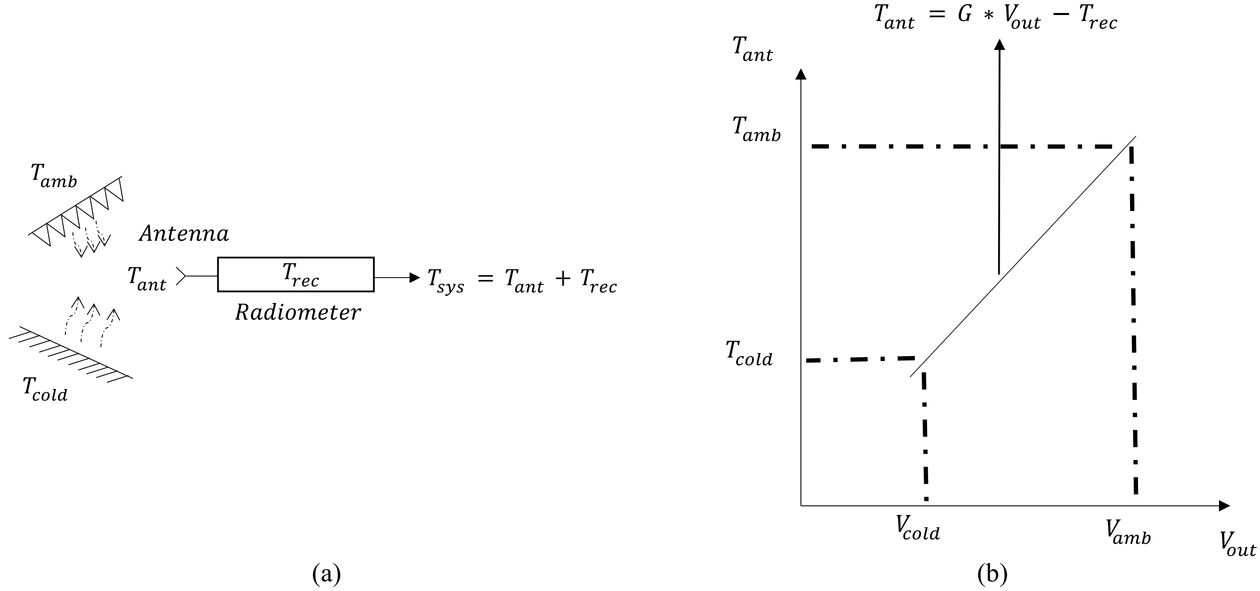

Fig. 1. Radiometer calibration. (a) Radiometer noise diagram. (b) Two-point radiometer calibration.

with the potential to perform the first temporal measurements of cloud and precipitation processes on a global basis [15]. The TEMPEST-D mission includes a five-channel millimeter-wave radiometer from 89 to 182 GHz, featuring cross-track scanning and end-to-end external calibration performed every two seconds using cosmic microwave background and an ambient blackbody target [16]. Next, the Time Resolved Observations of Precipitation structure and storm Intensity with a Constellation of SmallSats (TROPICS) led by the Massachusetts Institute of Technology Lincoln Laboratory is a 3U CubeSat planned to provide microwave measurements of tropical hurricanes and typhoons. The TROPICS will employ internal noise diode calibration as well as scanning vicarious sources to calibrate 12 radiometric channels from 90 to 206 GHz [17]. The TROPICS CubeSat constellation will be used to observe the thermodynamics of the troposphere and precipitation structure for storm systems. Finally, the Tropospheric Water and Cloud Ice (TWICE), led by CSU, is a 6U CubeSat instrument with millimeter and sub-millimeter-wave radiometers from 118 to 670 GHz [18]. TWICE is designed to enable measurements of cloud ice particle size distribution in the upper troposphere and lower stratosphere in addition to measuring water vapor profiles and liquid water retrievals. The TWICE total power radiometers will be calibrated using an on-orbit ambient calibration target and a cold-sky reflector.

This emerging field of CubeSats has introduced new challenges for microwave and millimeter-wave radiometry in terms of mass, volume, power consumption, and data telemetry rate. Another challenge for CubeSat radiometers is end-to-end calibration. External calibration targets are typically large in size and mass relative to radiometer antennas and optics. In addition, external calibration targets can limit the earth viewing portion of the scan or may reduce the number of available calibration measurements. In addition, it may be difficult to maintain homogeneous temperature distribution over the portion of the calibration target viewed by the radiometer antenna, as required for reliable calibration.

Recent advances in computational speed and deep learning neural network algorithms have significantly reduced the processing times and improved the accuracy of deep learning techniques [19]. This paper presents a new approach for microwave and millimeter-wave radiometer calibration by employing the advanced techniques of deep learning. The approach relies principally on the characterization of the radiometric instrument under various operating conditions to train a network of artificial neurons to predict the radiometer response.

In this paper, the noise-wave model representation of a radiometer will be used to demonstrate deep learning calibration. The noise-wave model is useful since it permits analysis of each component of the radiometer utilizing the scattering matrices to calculate the end-to-end flow of the noise as a signal [20]. The data generated by the noise-wave model will be used to train the artificial neural network (ANN) for the calibration algorithm. Independently collected samples from the same model will be used to test the ANN performance for radiometer calibration. This approach is intended to be used to improve the calibration of radiometers in CubeSats as well as for any other radiometer platform.

II. Radiometric Calibration Overview

Assuming a linear system and no gain fluctuation due to 1/f noise, a radiometer response is defined by a two-point calibration using the ambient and cold external calibration targets of the instrument where the antenna temperature is estimated from the output voltage [3]. As shown in Fig. 1(a), the ambient and cold targets with known temperatures are measured by the radiometer to determine the antenna temperature-to-voltage response of the system plotted in Fig. 1(b) [21].

The need to improve the accuracy and reliability of the radiometers has led to the use of several methods

This article has been accepted for inclusion in a future issue of this journal. Content is final as presented, with the exception of pagination.

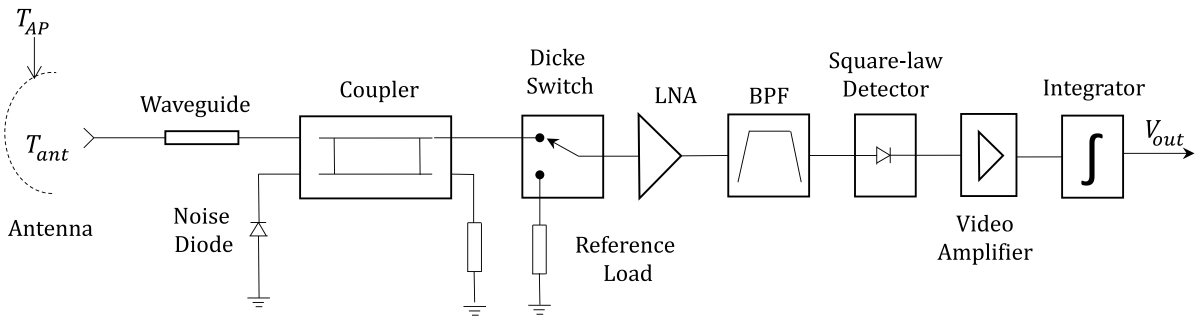

Fig. 2. Dicke-switching direct detection radiometer.

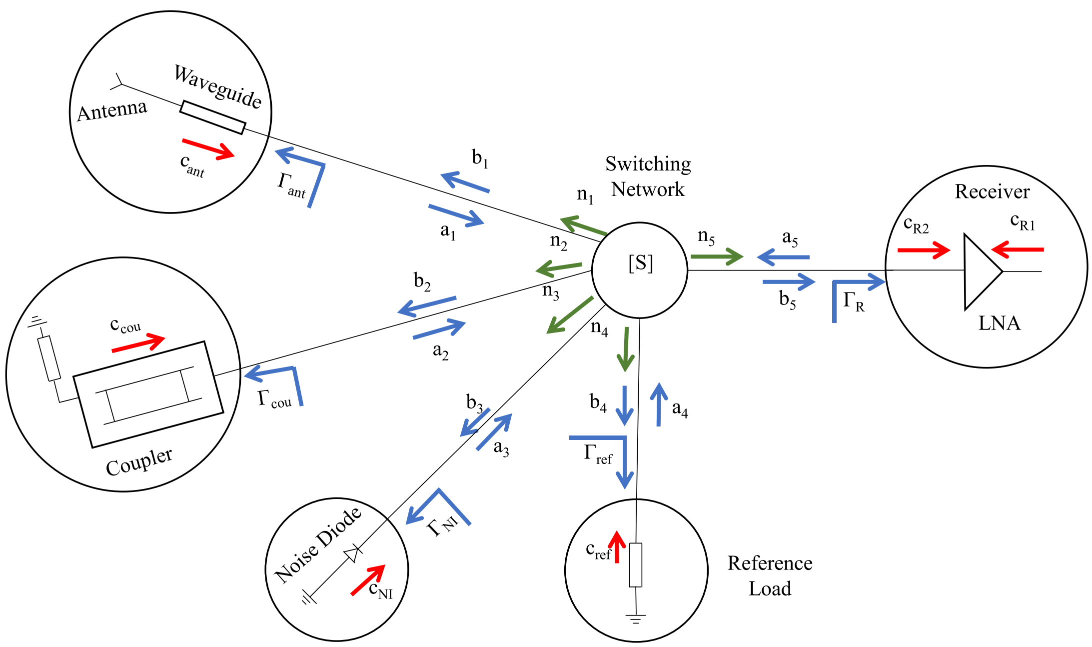

Fig. 3. Wave model representation of a radiometer. It should be noted that this is not a connection diagram.

to overcome gain fluctuation by employing internal gain calibration techniques [22] including noise diodes and reference loads, at the expense of radiometric resolution [1]. For instance, noise injection radiometers add a preset noise into the measurement path and Dicke radiometers switch the input signal between antenna and a reference source, which reduces the amount of time available for observation [3].

Internal gain calibration techniques used together with external calibration targets for two-point radiometric calibration improve accuracy and stability of a radiometer. However, it is a challenge to employ external calibration techniques in small satellites for end-to-end calibration due to their stringent design requirements on mass and volume [13]. However, complete end-to-end radiometric calibration cannot be accomplished by using only internal reference sources since the calibration source is inside the system after the antenna and will not account for its efficiency. In addition, internal calibration techniques add complexity to small satellites in terms of power and mass to control and maintain the thermal stability of those calibration sources.

This paper presents a deep learning approach for gain and radiometric calibration without making any assumptions regarding the system linearity, radiometer architecture, or presence of on-orbit external calibration targets.

III. Radiometer Wave Model

A Dicke-switching direct detection radiometer has been used to provide a generalized idea that can be applied to any architecture. The radiometer block diagram is shown in Fig. 2. The incident energy upon the antenna is denoted by the apparent antenna temperature distribution (T_{AP}) perceived as T_{ant} by the antenna that is measured as V_{out} at the output of the receiver.

The noise in the radiometer is characterized with noise waves since they allow the use of scattering matrices and signal flow graph theory for noise calculations [23], [24]. Fig. 3 illustrates the noise-wave diagram of the radiometer shown in Fig. 2. The connections of each block on this diagram are made to ease the understanding of the noise waves propagating in the system. Fig. 3 is not intended to show the physical connections of the system.

In the noise-wave representation, $\overline{a}$ (5×1) and $\overline{b}$ (5×1) are the incident and outgoing waves, respectively, to the switching network, defined over a 1-Hz bandwidth. The scattering matrix

This article has been accepted for inclusion in a future issue of this journal. Content is final as presented, with the exception of pagination.

is given as $\overline{\overline{S}}$ (5 × 5), and the internally generated noise waves are represented by $\overline{n}$ (5 × 1). The outgoing waves are defined as the sum of the scattered incident waves and the internally generated noise [20]

$$\overline{b} = \overline{\overline{S}}\,\overline{a} + \overline{n}. \tag{1}$$

Similarly, the incident waves ($\overline{a}$) are represented as the sum of the reflected incoming waves and the source waves ($\overline{a}_s$) [25]

$$\overline{a} = \overline{\overline{\Gamma}}\,\overline{b} + \overline{a}_s \tag{2}$$

where $\overline{\overline{\Gamma}}$ is a diagonal matrix such that each main diagonal element of the matrix represents the reflection coefficient looking into the port

$$\overline{\overline{\Gamma}} = \mathrm{diag}([\Gamma_{\mathrm{ant}} \quad \Gamma_{\mathrm{cou}} \quad \Gamma_{\mathrm{NI}} \quad \Gamma_{\mathrm{ref}} \quad \Gamma_R]). \tag{3}$$

The source waves ($\overline{a}_s$) in (2) are

$$\overline{a}_s = [c_{\mathrm{ant}} \quad c_{\mathrm{cou}} \quad c_{\mathrm{NI}} \quad c_{\mathrm{ref}} \quad c_{R1}]^T \tag{4}$$

where c_{ant} is the noise collected by the antenna from the scene, c_{cou} is the noise generated by the internal matched load of the coupler, c_{NI} is the noise generated by the noise diode and injected by the coupler, c_{ref} is the noise generated by the reference load, and c_{R1} is the noise generated by the receiver toward its input.

The final goal of the noise-wave calculations of the radiometer is to derive a relationship relating the input temperature and noise temperatures of various components of the radiometer to the output voltage that is needed for radiometer calibration analysis. The outgoing waves are represented in terms of the source waves by using (2) in (1) as

$$\begin{aligned} \overline{b} &= \overline{\overline{S}}\,\overline{a} + \overline{n} = \overline{\overline{S}}(\overline{\overline{\Gamma}}\,\overline{b} + \overline{a}_s) + \overline{n} \\ &= \overline{\overline{S}}\,\overline{\overline{\Gamma}}\,\overline{b} + \overline{\overline{S}}\,\overline{a}_s + \overline{n} \end{aligned} \tag{5}$$

$$\overline{b} - \overline{\overline{S}}\,\overline{\overline{\Gamma}}\,\overline{b} = \overline{\overline{S}}\,\overline{a}_s + \overline{n} \tag{6}$$

$$(\overline{\overline{I}} - \overline{\overline{S}}\,\overline{\overline{\Gamma}})\overline{b} = \overline{\overline{S}}\,\overline{a}_s + \overline{n} \tag{7}$$

where $\overline{\overline{I}}$ is a 5 × 5 identity matrix. Then

$$\overline{b} = (\overline{\overline{I}} - \overline{\overline{S}}\,\overline{\overline{\Gamma}})^{-1}(\overline{\overline{S}}\,\overline{a}_s + \overline{n}). \tag{8}$$

Now, a new variable is defined to ease the representation of these equations

$$\overline{\overline{\Lambda}} \stackrel{\mathrm{def}}{=} (\overline{\overline{I}} - \overline{\overline{S}}\,\overline{\overline{\Gamma}})^{-1} \tag{9}$$

$$\overline{b} = (\overline{\overline{I}} - \overline{\overline{S}}\,\overline{\overline{\Gamma}})^{-1}(\overline{\overline{S}}\,\overline{a}_s + \overline{n}) = \overline{\overline{\Lambda}}(\overline{\overline{S}}\,\overline{a}_s + \overline{n}) \tag{10}$$

$$\overline{b} = \overline{\overline{\Lambda}}\,\overline{\overline{S}}\,\overline{a}_s + \overline{\overline{\Lambda}}\,\overline{n}. \tag{11}$$

With the addition of the noise waves at the input of the amplifier, the input waves are represented as [26]

$$\overline{b'} = \overline{b} + \overline{c} \tag{12}$$

b' in (12) is the equivalent total input wave and $\overline{c}$ stands for the noise waves at the input of the low-noise amplifier (LNA) and defined as

$$\overline{c} = [0 \quad 0 \quad 0 \quad 0 \quad c_{R2}] \tag{13}$$

where c_{R2} is the noise generated by the receiver at the input of LNA.

The waves at the output of the LNA before the filter and the can be written as

$$\overline{b''} = S_{21}^{\mathrm{LNA}}\,\overline{b'} \tag{14}$$

where S_{21}^{LNA} is the forward transmission scattering matrix parameter of the LNA. The gain of the amplifier is represented in terms of the S-parameters of the amplifier as [1]

$$G = \left|S_{21}^{\mathrm{LNA}}\right|^2. \tag{15}$$

The power detected by the detector diode is the autocorrelation of the input waves at the input of the detector given by (14). The detector power can be written as the effect of the filter on the waves except that the bandwidth limiting is ignored [24], [26]

$$\langle b''(b'')^H \rangle = G\langle b'(b')^H \rangle \tag{16}$$

$$\langle b''(b'')^H \rangle = G\overline{\overline{N}} \tag{17}$$

where $\overline{\overline{N}}$ is defined as the correlation matrix of the input waves. Then, the voltage detected by the square-law detector is given as [1], [24]

$$V_{\mathrm{det}} = C_d G \overline{\overline{N}}_{(5,5)} \tag{18}$$

where C_d is the constant (responsivity) of the power detector. The voltage at the output of the video amplifier is

$$V_{\mathrm{video}} = G_{\mathrm{VA}} C_d G \overline{\overline{N}}_{(5,5)} \tag{19}$$

where G_{VA} is the gain of the video amplifier (V/V). The voltage at the output of the low-pass filter that is to be digitized by the radiometer back end can be written as

$$V_{\mathrm{LPF}} = g_{\mathrm{LPF}} G_{\mathrm{VA}} C_d G \overline{\overline{N}}_{(5,5)} \tag{20}$$

where g_{LPF} is the attenuation (i.e., expressed as gain) of the low-pass filter. Finally, the noise matrix $\overline{\overline{N}}$ needs to be represented in terms of temperature to reach our goal in noise-wave analysis for calibration analysis. In this paper, the Raleigh–Jeans limit of the Planck function is used [3]. Therefore, the noise waves over a 1-Hz bandwidth are expressed as a product of Boltzmann's constant (k_B) and the physical temperature (T) [23]. The equivalent input total wave defined in (12) and its Hermitian is given as

$$\overline{b'} = \overline{\overline{\Lambda}}\,\overline{\overline{S}}\,\overline{a}_s + \overline{\overline{\Lambda}}\,\overline{n} + \overline{c} \tag{21}$$

$$\begin{aligned} (\overline{b'})^H &= \left(\overline{\overline{\Lambda}}\,\overline{\overline{S}}\,\overline{a}_s + \overline{\overline{\Lambda}}\,\overline{n} + \overline{c}\right)^H \\ &= \overline{a}_s^H\,\overline{\overline{S}}^H\,\overline{\overline{\Lambda}}^H + \overline{n}^H\,\overline{\overline{\Lambda}}^H + \overline{c}^H. \end{aligned} \tag{22}$$

Then, the correlation matrix of input noise waves given in (17) is calculated as

$$\bar{\bar{N}} = \langle b'(b')^H \rangle \tag{23}$$

$$\bar{\bar{N}} = \langle (\bar{\bar{\Lambda}}\bar{\bar{S}}\bar{a}_s + \bar{\bar{\Lambda}}\bar{n} + \bar{c}) \cdot (\bar{a}_s^H \bar{\bar{S}}^H \bar{\bar{\Lambda}}^H + \bar{n}^H \bar{\bar{\Lambda}}^H + \bar{c}^H) \rangle \tag{24}$$

$$\begin{aligned} \bar{\bar{N}} = {} & \bar{\bar{\Lambda}}\bar{\bar{S}}\langle \bar{a}_s \bar{a}_s^H \rangle \bar{\bar{S}}^H \bar{\bar{\Lambda}}^H + \bar{\bar{\Lambda}}\langle \bar{n}\, \bar{a}_s^H \rangle \bar{\bar{S}}^H \bar{\bar{\Lambda}}^H \\ & + \langle \bar{c}\, \bar{a}_s^H \rangle \bar{\bar{S}}^H \bar{\bar{\Lambda}}^H + \bar{\bar{\Lambda}}\bar{\bar{S}}\langle \bar{a}_s \bar{n}^H \rangle \bar{\bar{\Lambda}}^H \\ & + \bar{\bar{\Lambda}}\langle \bar{n}\, \bar{n}^H \rangle \bar{\bar{\Lambda}}^H + \langle \bar{c}\, \bar{n}^H \rangle \bar{\bar{\Lambda}}^H \\ & + \bar{\bar{\Lambda}}\bar{\bar{S}}\langle \bar{a}_s \bar{c}^H \rangle + \bar{\bar{\Lambda}}\langle \bar{n}\, \bar{c}^H \rangle + \langle \bar{c}\, \bar{c}^H \rangle. \end{aligned} \tag{25}$$

The noise matrix in (25) is represented in terms of the correlation of the noise waves. The noise matrix is further simplified by employing Bosma's theorem [27] and following the theorems presented in [1], [23], [24], and [25]:

$$\begin{aligned} \bar{\bar{N}} = {} & \bar{\bar{\Lambda}}\bar{\bar{S}} k_B \bar{\bar{T}}_s \bar{\bar{S}}^H \bar{\bar{\Lambda}}^H \\ & + \bar{\bar{\Lambda}} k_B T_{\mathrm{SN}} (\bar{\bar{I}} - \bar{\bar{S}}\,\bar{\bar{S}}^H) \bar{\bar{\Lambda}}^H + k_B \bar{\bar{C}} \end{aligned} \tag{26}$$

$$\bar{\bar{N}} = k_B [\bar{\bar{\Lambda}}\bar{\bar{S}}\,\bar{\bar{T}}_s \bar{\bar{S}}^H \bar{\bar{\Lambda}}^H + \bar{\bar{\Lambda}} T_{\mathrm{SN}} (\bar{\bar{I}} - \bar{\bar{S}}\,\bar{\bar{S}}^H) \bar{\bar{\Lambda}}^H + \bar{\bar{C}}] \tag{27}$$

$$\bar{\bar{T}}_{\mathrm{RAD}} \stackrel{\mathrm{def}}{=} [\bar{\bar{\Lambda}}\bar{\bar{S}}\,\bar{\bar{T}}_s \bar{\bar{S}}^H \bar{\bar{\Lambda}}^H + \bar{\bar{\Lambda}} T_{\mathrm{SN}} (\bar{\bar{I}} - \bar{\bar{S}}\,\bar{\bar{S}}^H) \bar{\bar{\Lambda}}^H + \bar{\bar{C}}] \tag{28}$$

$$\bar{\bar{N}} = k_B \bar{\bar{T}}_{\mathrm{RAD}} \tag{29}$$

where T_{SN} is the physical temperature of the Dicke switch, $\bar{\bar{C}}$ is the diagonal correlation noise matrix of the LNA, which depends on its physical temperature (T_{LNA}), and ($\bar{\bar{T}}_s$) is the temperature matrix defined as

$$\bar{\bar{T}}_s = \mathrm{diag}[T_A \quad T_{\mathrm{cou}} \quad T_{\mathrm{NI}} \quad T_{\mathrm{ref}} \quad T_R] \tag{30}$$

where T_A is the antenna physical temperature, T_{cou} is the noise temperature of the matched load of the coupler, T_{NI} is the equivalent noise temperature injected thorough the noise diode, T_{ref} is the physical temperature of the reference load, and T_R is the physical temperature of the isolator at the input of the LNA. Finally, using (20), the analog voltage digitized by the radiometer back end is expressed as

$$V_{\mathrm{LPF}} = k_B g_{\mathrm{LPF}} G_{\mathrm{VA}} C_d \mathrm{GB} \bar{\bar{T}}_{\mathrm{RAD}_{(5,5)}} \tag{31}$$

where G is the gain of the LNA (V/V), C_d is detector diode constant (V/W), G_{VA} is the gain of the video amplifier (V/V), and B is the bandwidth (Hz).

IV. Radiometer Deep Learning Model For Calibration

The proposed model for radiometric calibration is based on a multilayer perceptron (MLP) feed-forward ANN utilizing a supervised deep learning algorithm to retrieve antenna temperatures from the voltage measurements at the output of the radiometer. The multiple-layer structure of the deep MLP model and the nonlinear activation between layers make this option suitable for extraction of features to learn representations of complex radiometer data structure with multiple levels of abstraction [19], [28].

The internal adjustable parameters of the MLP structure are the weights that define the input–output relationship of the network. A learning algorithm adjusts the weights of the network by minimizing the error of the cost function between the output and the desired values. The stochastic gradient descent (SGD) algorithm computes the average gradient by calculating the outputs and the errors for a few examples of large data sets to adjust the weights, resulting in frequent updates of those parameters with high variance. As a result, the loss function fluctuates due to high variance that helps the detection of different local minima for the SGD gradient calculation. In this way, the SGD significantly reduces computational time and memory usage while providing fast convergence for the training [29].

A neuron is the smallest computational unit in the neural network architecture. The data at the input of a neuron are transmitted to its output through activation functions, which define the system response of a single neuron to specific information at its input. The rectified linear unit (ReLU) nonlinear activation function is a half-wave rectifier defined as

$$f(x) = \max(0, x) \tag{32}$$

where x is the input to a neuron in the network and $f(x)$ is the output of the neuron. The simple structure of the ReLU activation function compared to complex activation functions, including sigmoid and hyperbolic tangent, provides fast learning in multiple layer networks allowing deep supervised learning without unsupervised pretraining [30], [31].

The number of layers and neurons at each layer in the MLP network depends on the complexity and nonlinearity of the calibration problem. These values are found after an optimization process, and they are specific to the subjacent hardware being calibrated and the amount of available information, such as inputs and data set. Increasing the number of layers increases the amount of nonlinearity in the system. The network can learn complex data structures with multiple levels of abstraction by increasing the number of layers and neurons. However, having higher level of complexity than is needed in the neural network model may result in slow convergence or not being able to converge to the desired performance.

The following procedure is suggested to build a deep-learning radiometer calibrator.

1) Analyze the calibration problem from the point of view of a neural network.
2) Start the design with a reasonable number of layers and neurons.
3) Determine if the calibrator is ready for the radiometer calibration or it requires improvement by examining the error function and convergence rate of the calibrator. If the performance does not meet the specifications, the designer has several options to improve it, i.e., going back to Step 2, considering including other sources of information as NN inputs, or extending the data set to make it more statistically comprehensive.

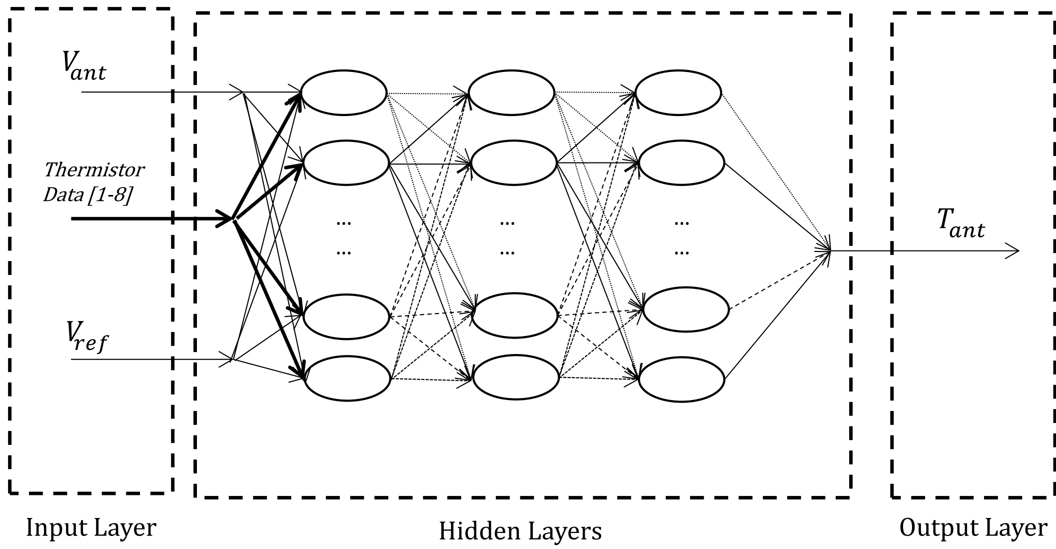

Fig. 4. ANN architecture for radiometer calibration used for the presented model.

The designed MLP neural network structure for the calibration problem contains three hidden layers as depicted in Fig. 4. The measured radiometer antenna temperature is the final product of the ANN to be retrieved from the radiometer antenna and reference voltage measurements in addition to thermal measurements of the instrument.

The noise-wave model of a radiometer is used to generate data for the MLP network since the noise-wave representation of radiometers provides flexibility to introduce uncertainty and noise into the system for testing the performance of the calibration process under various conditions. In addition, the noise-wave model breaks down the radiometer architecture into a number of smaller parts, making it easier to calculate the noise waves originating from each separate part of the instrument [24].

The ANN uses the antenna temperature data for target values in the supervised learning of the system for training. As shown in Fig. 4, the ANN model has three types of inputs.

1) V_{ant} is the radiometer voltage output when the antenna leg is selected by the Dicke switch.
2) V_{ref} is the radiometer voltage output when the Dicke switch is set to the reference load leg.
3) Thermistor data, which consists of the acquired physical temperature of the antenna, waveguide, noise diode, coupler, switch, reference load, isolator, and receiver electronics measured by the thermistors mounted on those subsystems. The input information from the thermistors is useful to understand the radiometer noise change with respect to physical temperature due to orbital variations, e.g., in the sunlight compared to earth eclipse.

The ANN model builds a relationship between the input and the output layers by assigning suitable coefficients to each neuron in each hidden layer. In this way, the model performs end-to-end calibration of the radiometer.

Common calibration strategies use a Dicke load or noise diodes to improve system stability for radiometric measurements. Then, two-point calibration is performed using measurements of hot and cold calibration targets to convert measured counts to volts [3]. However, the proposed model calibrates the instrument in a single step by directly providing the calibrated antenna temperature from the measurements, as opposed to conventional two-point calibration techniques in which the antenna temperature is estimated in two steps.

V. Deep Learning Calibration Results

The proof of concept of the deep learning MLP model that has been developed for calibration will be carried out by using the radiometer noise-wave model derived in this paper. The radiometer chosen for this paper is a basic Dicke radiometer. The input parameters for such a radiometer are presented in Table I. The radiometer is assumed to be operating in low-earth orbit conditions. It is also assumed that the temperature control of the system to keep the radiometer instrument at a constant temperature still depends upon the external temperature since the CubeSat has stringent limitations for power and mass. Therefore, the temperature of each part of the radiometer system varies at a different rate due to orbital temperature fluctuations.

The orbital and radiometer operation parameters are provided in Table II. Several data sets have been calculated from the noise-wave model under the orbital conditions provided in Table II. Then, as a rule of thumb defined by the holdout method for an MLP neural network data set selection, 70% of the samples of the data set have been randomly selected for the training of the neural network [32]. The remaining samples are allocated for the testing and validation of the ANN.

The first test is the noise-free case where there is no uncertainty in the measurements of the antenna voltage from the radiometer for both the training and testing data sets. In addition, the thermistors perform precise measurements of the thermal state of the subsystems (i.e., assuming that they do not have any uncertainty or bias). The goal of the noise-free test is to examine the performance of the calibration ANN under ideal conditions.

TABLE I

PARAMETERS OF A TYPICAL DICKE-SWITCH DIRECT DETECTION MICROWAVE RADIOMETER SHOWN IN FIG. 2 [1], [22], [24], [26]. IT SHOULD BE NOTED THAT THE INPUT PARAMETERS HAVE A MUCH WIDER RANGE THAN THAT OF A CONVENTIONAL RADIOMETER

Parameter	**Value**
Antenna Reflection Coefficient	0.03
Antenna Loss	0.05 dB
Waveguide Loss	0.05 dB
Coupling Factor	15 dB
Excess Noise Ratio (ENR) of Noise Diode	25 dB ± 0.01 dB/K
Directivity of Coupler	20 dB
Return Loss from the Dicke Load	30 dB
Isolation of the Dicke Switch	25 dB
Insertion Loss of the Dicke Switch	0.15 dB
Return Loss of the Dicke Switch	23 dB
LNA Reflection Coefficient	0.03
Power Detector Constant	2300 (V/W)

TABLE II

ORBITAL AND RADIOMETRIC OPERATION PARAMETERS

Parameter	**Value**
Antenna temperature range	From 2.7 K to 350 K
Orbital temperature range	From 233 K to 353 K
LNA gain variation	± 2.5 dB

The ANN is trained using random selected training samples. Then, the antenna temperature of the radiometer has been predicted by the ANN using 20 000 randomly selected samples from the testing data set. Fig. 5 shows a 5-K bin plot of the ANN predicted antenna temperatures versus the target antenna temperatures calculated from the noise-wave model of the radiometer. The root-mean-square error (RMSE) and the standard deviation in the predictions are calculated as 48 mK.

However, the output voltage of an actual radiometer has uncertainty due to noise in the system as well as limited bandwidth and integration time [3]. The radiometric resolution of a total power radiometer is

$$\Delta T = \frac{T_{\text{sys}}}{\sqrt{\text{BW} \times \tau_{\text{int}}}} \tag{33}$$

where T_{sys} is the system noise temperature (K), BW is the equivalent noise bandwidth (Hz) of the radiometer, and τ_{int} is the integration time (s) [22].

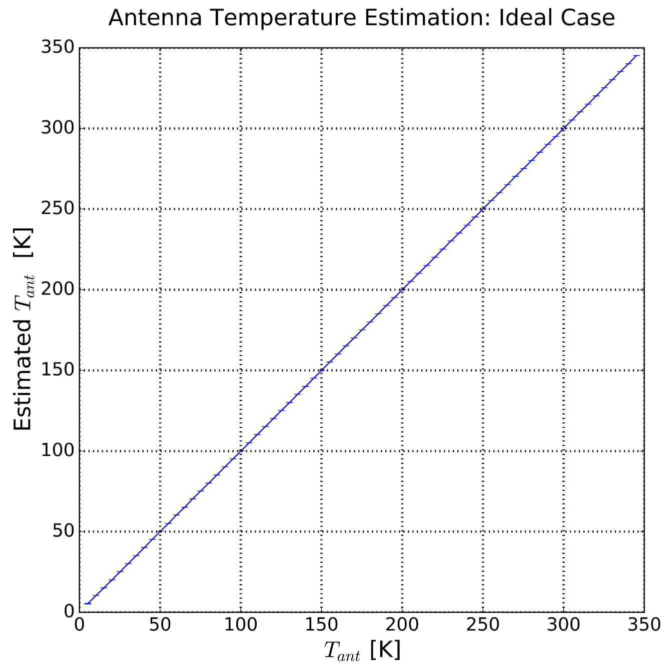

Fig. 5. Comparison of antenna temperature estimated using the ANN model with the true temperatures for an ideal case.

The goal of noise-added testing is to study the performance of the designed ANN for calibration under the presence of noise in the system. The noise-wave model is used to generate 348 000 testing samples when the antenna is measuring targets with temperatures from 2.7 to 350 K with 1-K resolution. Before applying these testing samples to the ANN for calibration, 0.1% zero-mean additive white Gaussian random noise is introduced into the radiometer output voltage measurements. The output voltage uncertainty of 0.1% accounts for gain fluctuations and corresponds to 0.3 K of uncertainty at an antenna temperature of 300 K. The same test is repeated for the uncertainty level of 0.3% at the radiometer voltage output (i.e., $\Delta T = 0.9$ K at $T_{\text{ant}} = 300$ K).

The resulting sensitivity of radiometric temperatures to antenna voltage measurements is defined by

$$\Delta T / \Delta V = \frac{T_{\max} - T_{\min}}{V_{\max} - V_{\min}} \tag{34}$$

where $V_{\max}$ and $V_{\min}$ are the output voltage readings at the maximum ($T_{\max}$) and minimum ($T_{\min}$) temperature measurement during the test. Then, the output voltage uncertainty is expressed in terms of antenna temperature uncertainty as

$$\Delta T_{\text{noise}} = (\Delta T / \Delta V\ ) \times \Delta V_{\text{noise}}. \tag{35}$$

The expected uncertainty in the temperature in (35) is ΔT_{noise}, and ΔV_{noise} is the amount of uncertainty present at the measured output voltage of the radiometer represented in Volts.

The expected and measured uncertainties in Kelvin when using the ANN for antenna temperature calibration for 0.1% uncertainty at the received radiometer output voltage are plotted with a bin size of 5 K, as presented in Fig. 6(a). As shown in the plot, the measured noise is in agreement

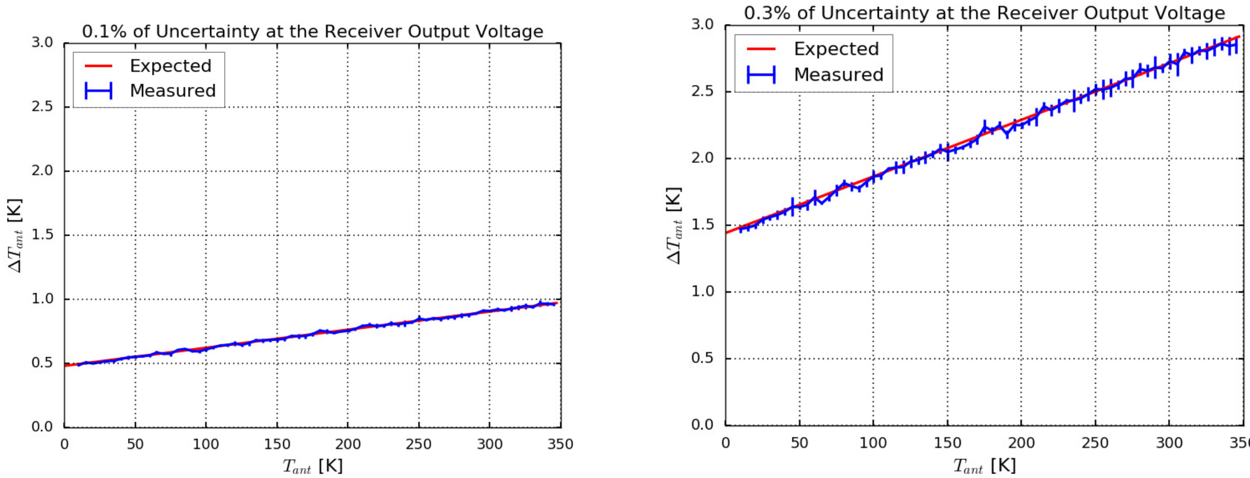

(a) (b)

Fig. 6. Antenna temperature estimated using the ANN model when (a) 0.1% uncertainty is presented in the output voltage and (b) 0.3% uncertainty is presented in the output voltage.

with the expected noise. We conclude that the ANN model does not add any significant noise to the retrievals.

In Fig. 6(b), the radiometer output voltage uncertainty is increased to 0.3%. Similar to the results for 0.1% of the uncertainty level, the measured noise level agrees with the expected value. The test results for the ideal situation and the case with uncertainty in the radiometer output voltage indicate that the designed ANN model does not add any significant noise to radiometer calibration.

A radiometer operating in orbit has also inaccuracies in the acquired physical temperature information as a result of digitization and measurement errors. Therefore, in addition to 0.1% output voltage uncertainty, 0.1-K uncertainty in the thermal data is introduced to 20 000 randomly selected samples of testing data. The current level of thermistor technology allows a physical temperature measurement precision of better than 0.1 K [33]. The estimated antenna temperatures of the ANN have been plotted with respect to expected antenna temperatures on Fig. 7. The RMSE has been calculated as 0.75 K for the antenna temperature estimates for this case.

Several randomly selected training sample data sets with various resolutions are generated using the noise-wave model to analyze the effect of the training data set resolution on the ANN estimates. Each training data set with sample size from 1.2 million to 149 million is input to an ANN having the same structure as presented in Fig. 4 to train for radiometer calibration. Each trained network for five epochs has been tested with the same three randomly selected data sets having 20 000 noise-free samples, with 0.1% and 0.3% radiometer output voltage uncertainty. The results are summarized in Table III with the expected RMSE values for noise free, 0.1% and 0.3% uncertainty test cases in addition to expected standard deviation (STD) values calculated at 300 K for 0.1% and 0.3% uncertainty test cases.

The RMSE and STD results provide a complete picture of the ANN performance since the RMSE is used to analyze how close the estimates are to the expected values while the STD provides information about how much uncertainty exists around the mean estimate value. The measured RMSE values are close to the expected ones for the networks trained with larger numbers of the samples. This indicates that increasing the number of training samples improves the performance of the network to estimate the antenna temperatures for the networks having the same training epoch numbers. The measured and expected STD values are close to the expected results, confirming that the ANN does not add any significant noise when it is tested with networks having a different number of training samples.

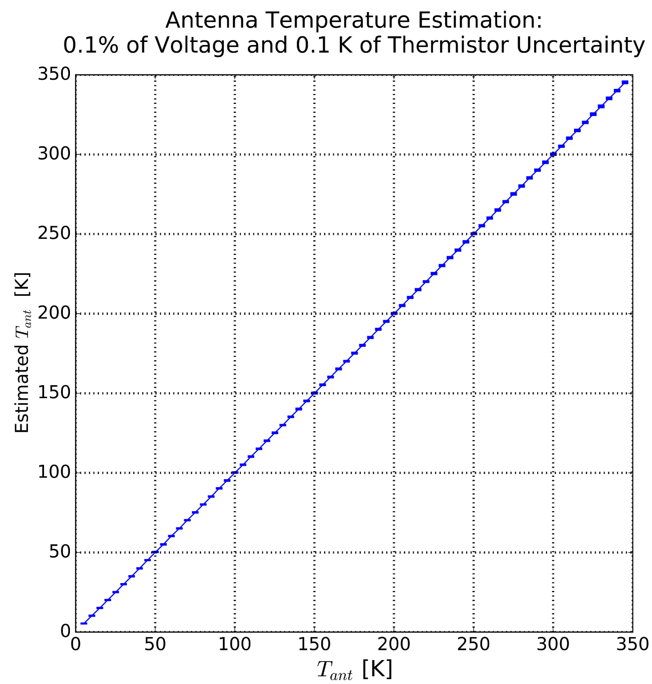

Fig. 7. Antenna temperature estimates using the ANN model for a radiometer with 0.1% output voltage and 0.1-K thermistor reading uncertainties compared with the true temperatures.

TABLE III

MEASURED RMSE AND STD PERFORMANCE FOR THE ANTENNA TEMPERATURE RETRIEVALS OF THE ANNS TRAINED FOR FIVE EPOCHS WITH DIFFERENT NUMBERS OF SAMPLES

# OF TRAINING SAMPLES (MILLIONS)	**RMSE [2.7-350] K**			**STD @ 300 K**	
	EXPECTED RMSE: 0 K	EXPECTED RMSE: 0.73 K	EXPECTED RMSE: 2.18 K	EXPECTED STD: 0.9 K	EXPECTED STD: 2.71 K
149	0.09	0.74	2.23	0.90	2.72
15	0.11	0.76	2.22	0.90	2.76
6.2	0.11	0.75	2.22	0.93	2.75
3.1	0.60	0.97	2.32	0.92	2.84
1.2	1.46	1.64	2.68	0.91	2.79

TABLE IV

MEASURED RMSE PERFORMANCE FOR THE ANTENNA TEMPERATURE RETRIEVALS OF THE ANNS TRAINED FOR DIFFERENT NUMBERS OF TRAINING EPOCHS

# OF TRAINING EPOCHS	**RMSE [2.7-350] K**		
	EXPECTED RMSE: 0 K	EXPECTED RMSE: 0.73 K	EXPECTED RMSE: 2.18 K
5	1.46	1.64	2.68
10	0.80	1.10	2.40
20	0.16	0.76	2.25
40	0.05	0.75	2.23

TABLE V

MEASURED RMSE PERFORMANCE FOR THE ANTENNA TEMPERATURE ESTIMATES OF THE ANNS TRAINED WHEN DIFFERENT AMOUNTS OF UNCERTAINTY IS INTRODUCED TO THE TRAINING SAMPLES

NOISE LEVEL OF TRAINING DATASET	**RMSE [2.7-350] K**		
	EXPECTED RMSE: 0 K	EXPECTED RMSE: 0.73 K	EXPECTED RMSE: 2.18 K
0 (NOISE FREE)	0.048	0.75	2.23
0.1% OF UNCERTAINTY	0.068	0.75	2.23
0.3% OF UNCERTAINTY	0.195	0.77	2.23

The performance of the ANN for the accuracy of the estimates also depends on how well the network has learned during the training process [19]. The epoch number of the network for training defines how many times the training process is repeated using the complete training data samples. Therefore, the number of epochs used to train the neural network is expected to affect the performance of the retrievals. To demonstrate the effect of training epochs on the accuracy of the estimates, the trained ANN with the lowest number of training samples among those ANNs listed in Table III is chosen. The developed noise-wave model for the Dicke radiometer is used to generate 1.2 million randomly selected training samples to train several ANNs, each having different training epochs but the same training data set. Then, each network has been tested with the same randomly selected 20 000 testing samples. The results are summarized in Table IV. The accuracy of the retrievals significantly improves when the number of training epochs is increased. However, it is evident from the results that any further increase of the training epochs beyond 20 does not have significant improvement in the performance of the ANN for the tested calibration model.

The data used for training an ANN will have measurement uncertainty since it will be obtained from a real radiometer even if the radiometer is operating in a controlled environment in laboratory conditions. Therefore, uncertainty has been introduced into the voltage measurements obtained from the noise-wave model for training the ANN calibration model. The radiometer noise-wave model has been used to generate three randomly selected training data sets with noise-free, 0.1% and 0.3% of uncertainty, respectively. The ANN calibration model is trained for 40 training epochs using each of those three training data sets separately with 1.2 million training samples. The results are summarized in Table V. The trained ANNs have similar performance when they are tested with samples having 0.1% and 0.3% of uncertainty. Finally, this test has shown that introducing uncertainty into the samples for training the ANN does not have a significant effect on the estimates, when compared to noise-free cases shown in Table IV.

In microwave and millimeter-wave radiometry, it is desirable to have a linear calibration curve, as shown in Fig. 1(b), to perform reliable measurements in orbit with high accuracy. However, radiometers have nonlinear temperature to voltage response, as shown in Fig. 8(a), due to imperfections in square-law detector diodes, amplifiers, and analog-to-digital converters. The detector diodes have a square-law transfer function for the most of the radiometer's operating range, except for low-signal detection. In addition, the third-order

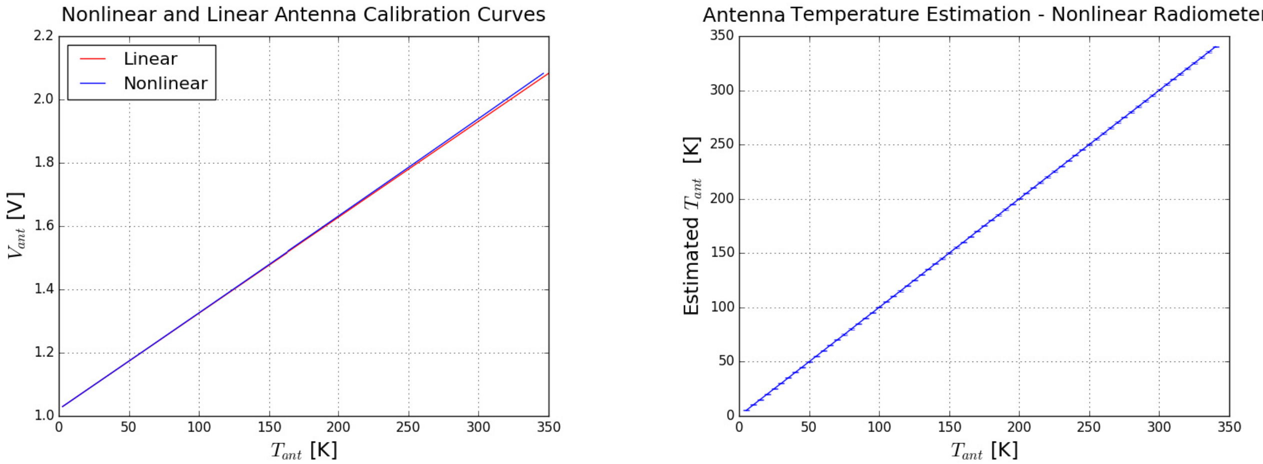

(a) (b)

Fig. 8. ANN calibration performance. (a) Nonlinear and linear antenna calibration curves and (b) antenna temperature estimates using the ANN model for a nonlinear radiometer.

intercept of the RF amplifiers and fourth-order RF coefficient of the video amplifier contribute to the nonlinear behavior of radiometers [34]. There are several ground-based calibration methods to check the linearity of a radiometer, including three-point calibration and slope methods explained in [22]. However, those methods are not suitable to be used in on-orbit radiometers.

The noise-wave model is used to generate data for a radiometer having a nonlinear calibration curve to check the performance of the ANN model regarding linearity. The voltage-to-temperature calibration curve for such a radiometer is given in Fig. 8(a). The ANN model is trained by randomly selected 2 millions of training samples having 2 K of nonlinearity at 250-K antenna temperature and 0.1% radiometer output voltage uncertainty. The trained network is tested using 50 000 randomly selected samples. The estimated antenna temperatures are plotted with 5-K bin size with respect to ground-truth antenna temperatures in Fig. 8(b). The RMSE of the ANN calibration is calculated as 0.3 K. These results indicate that a radiometer having nonlinear calibration response can be calibrated on orbit by applying the ANN model.

The ANN tests have been applied for an ideal radiometer, a radiometer having various uncertainties in the output voltage, and the thermistor measurements as well as a radiometer with a nonlinear radiometer response. The results have shown that the ANN model reliably performs low-noise radiometer calibration under various conditions.

VI. Discussion and Conclusion

The proposed method of calibration for microwave and millimeter-wave radiometers is based on the deep learning ANN computation technique. This technique has been demonstrated using the radiometer noise-wave model. It has been shown through calculations that the ANN model produces calibrated antenna temperatures at high accuracy (low RMSE value) directly, i.e., without any extra data provided by an external target or a noise diode, as outlined in Fig. 4. Furthermore, the demonstration has been performed for the case where there are large gain variations and insufficient temperature control, as shown in Tables II and III. The noise analysis of the model has shown that the ANN does not introduce any significant noise into the radiometric measurements, for a well-trained model. Therefore, the presented calibration model can be applied to calibrate microwave and millimeter-wave radiometers regardless of the architecture design, operating frequencies, and bandwidths.

The training data set for the ANN model can be obtained from thermal vacuum chamber (TVAC) radiometric measurements during the prelaunch phase of the instrument development. During TVAC tests, the antenna performs radiometric measurements when viewing a calibration target with a known and varying temperature in a controlled environment. While radiometric measurements are being performed, the temperature of different parts of the instrument is continuously recorded with thermistors placed on the instrument. During TVAC testing, one may place as many thermistors as possible on various parts of the instrument for synchronized temperature monitoring with the radiometric acquisitions since the tests are performed in laboratory environment. Then, it can be determined which parts are critical for deep learning calibration based on the radiometric measurements and thermistor readings during TVAC testing. Prelaunch tests may also provide an opportunity to analyze the system before launch in addition to providing data for the training.

This paper proposes a general approach that has been demonstrated for different numbers of training samples and training epochs. The number of samples for training should be estimated for any specific radiometer mission based on the mission requirements and orbital parameters. Then, the ANN architecture should be designed based on the complexity of the training data set. Finally, the ANN model should be trained for a sufficient number of training epochs with the training samples obtained during the prelaunch tests to achieve the desired performance for radiometer calibration.

The ANN model that has been trained for a specific mission can also be tuned while the radiometer is on-orbit with the provided data from internal calibration sources or from cold-sky measurements to consider any changes in the radiometer system parameters including the aging of the instrument. Also, external calibration sources that do not exist in the instrument can be used to tune the neural network in-orbit operation. For this purpose, the radiometer can perform measurements over the ocean surface or cold sky to improve the on-orbit performance of the deep learning calibration [35]. Furthermore, cross-calibration of the antenna temperature measurements is possible with another on-orbit radiometer performing nearly collocated measurements. This might also be used to retrain the ANN model to adjust the weights to improve on-orbit calibration [36], [37]. The proposed method can also be applied along with end-to-end calibration techniques. In this case, calibration using the ANN model may be used to correct estimates of calibration gain and receiver noise temperature.

The proposed study can be applied to the radiometers operated from other platforms such as airborne or ground-based systems. In addition, the technique presented in this paper may be extended to perform analysis for time-varying statistical fluctuations and biases in calibration reference temperatures.

References

[1] F. T. Ulaby, R. K. Moore, and A. K. Fung, *Microwave Remote Sensing: Active and Passive*, vol. 1. Reading, MA, USA: Addison-Wesley, 1981.

[2] L. Yujiri, M. Shoucri, and P. Moffa, "Passive millimeter wave imaging," *IEEE Microw. Mag.*, vol. 4, no. 3, pp. 39–50, Sep. 2003.

[3] P. Racette and R. H. Lang, "Radiometer design analysis based upon measurement uncertainty," *Radio Sci.*, vol. 40, no. 5, pp. 1–22, Oct. 2005.

[4] I. Corbella, A. J. Gasiewski, M. Klein, V. Leuski, A. J. Francavilla, and J. R. Piepmeier, "On-board accurate calibration of dual-channel radiometers using internal and external references," *IEEE Trans. Microw. Theory Techn.*, vol. 50, no. 7, pp. 1816–1820, Jul. 2002.

[5] A. B. Tanner and A. L. Riley, "Design and performance of a high-stability water vapor radiometer," *Radio Sci.*, vol. 38, no. 3, pp. 15-1–15-11, Jun. 2003.

[6] E. R. Westwater, "The accuracy of water vapor and cloud liquid determination by dual-frequency ground-based microwave radiometry," *Radio Sci.*, vol. 13, no. 4, pp. 677–685, Jul./Aug. 1978.

[7] J. R. Wang, P. E. Racette, and J. R. Piepmeier, "A comparison of near-concurrent measurements from the SSMIS and CoSMIR for some selected channels over the frequency range of 50–183 GHz," *IEEE Trans. Geosci. Remote Sens.*, vol. 46, no. 4, pp. 923–933, Apr. 2008.

[8] S. T. Brown *et al.*, "The high-altitude MMIC sounding radiometer for the global Hawk unmanned aerial vehicle: Instrument description and performance," *IEEE Trans. Geosci. Remote Sens.*, vol. 49, no. 9, pp. 3291–3301, Sep. 2011.

[9] C. Kummerow, I. M. Hakkarinen, H. F. Pierce, and J. A. Weinman, "Determination of precipitation profiles from airborne passive microwave radiometric measurements," *J. Atmos. Ocean. Technol.*, vol. 8, no. 1, pp. 148–158, 1991.

[10] N. C. Grody, "Remote sensing of atmospheric water content from satellites using microwave radiometry," *IEEE Trans. Antennas Propag.*, vol. AP-24, no. 2, pp. 155–162, Mar. 1976.

[11] L.-L. Fu *et al.*, "TOPEX/POSEIDON mission overview," *J. Geophys. Res.*, vol. 99, no. C12, pp. 24369–24381, Dec. 1994.

[12] Y. Rahmat-Samii, V. Manohar, and J. M. Kovitz, "For satellites, think small, dream big: A review of recent antenna developments for CubeSats.," *IEEE Antennas Propag. Mag.*, vol. 59, no. 2, pp. 22–30, Apr. 2017.

[13] The CubeSat Program, Cal Poly SLO, San Luis Obispo, CA, USA. (Feb. 2014). *CubeSat Design Specification Rev.13*. Accessed: May 14, 2018. [Online]. Available: http://www.cubesat.org

[14] The CubeSat Program. California Polytechnic State University, San Luis Obispo, CA, USA. (Apr. 2016). *6U CubeSat Design Specification Rev. PROVISIONAL*. Accessed: May 14, 2018. [Online]. Available: http://www.cubesat.org

[15] S. C. Reising *et al.*, "Overview of temporal experiment for storms and tropical systems (TEMPEST) cubesat constellation mission," in *IEEE MTT-S Int. Microw. Symp. Dig.*, Phoenix, AZ, USA, May 2015, pp. 1–4.

[16] S. C. Reising *et al.*, "Global measurement of temporal signatures of precipitation: Development of the temporal experiment for storms and tropical systems technology demonstration mission," in *Proc. IEEE Int. Geosci. Remote Sens. Symp. (IGARSS)*, Fort Worth, TX, USA, Jul. 2017, pp. 5931–5933.

[17] MIT Lincoln Laboratory, Massachusetts Institute of Technology. *Time-Resolved Observations of Precipitation Structure and Storm Intensity with a Constellation of Smallsats*. Accessed: May 14, 2018. [Online]. Available: https://tropics.ll.mit.edu/CMS/tropics/pdf/nasaTropicsFactSheet.pdf

[18] M. Ogut *et al.*, "Command and data handling (C&DH) subsystem for the tropospheric water and cloud ice (TWICE) 6U-class satellite instrument," in *Proc. IEEE Int. Geosci. Remote Sens. Symp. (IGARSS)*, Fort Worth, TX, USA, Jul. 2017, pp. 2744–2747.

[19] Y. LeCun, Y. Bengio, and G. Hinton, "Deep learning," *Nature*, vol. 521, pp. 436–444, May 2015.

[20] S. W. Wedge and D. B. Rutledge, "Wave techniques for noise modeling and measurement," *IEEE Trans. Microw. Theory Techn.*, vol. 40, no. 11, pp. 2004–2012, Nov. 1992.

[21] R. W. Saunders, T. J. Hewison, S. J. Stringer, and N. C. Atkinson, "The radiometric characterization of AMSU-B," *IEEE Trans. Microw. Theory Techn.*, vol. 43, no. 4, pp. 760–771, Apr. 1995.

[22] N. Skou and D. L. Vine, *Microwave Radiometer Systems: Design and Analysis*, 2nd ed. Norwood, MA, USA: Artech House, 2006.

[23] S. W. Wedge and D. B. Rutledge, "Noise waves and passive linear multiports," *IEEE Microw. Guided Wave Lett.*, vol. 1, no. 5, pp. 117–119, May 1991.

[24] A. Camps, "Noise wave analysis of Dicke and noise injection radiometers: Complete S parameter analysis and effect of temperature gradients," *Radio Sci.*, vol. 45, no. 5, pp. 1–9, Oct. 2010.

[25] J. Randa, "Noise characterization of multiport amplifiers," *IEEE Trans. Microw. Theory Techn.*, vol. 49, no. 10, pp. 1757–1763, Oct. 2001.

[26] I. Corbella *et al.*, "Analysis of correlation and total power radiometer front-ends using noise waves," *IEEE Trans. Geosci. Remote Sens.*, vol. 43, no. 11, pp. 2452–2459, Nov. 2005.

[27] H. Bosma, "On the theory of linear noisy systems," Ph.D. dissertation, Dept. Elect. Eng., Eindhoven Univ. Technol., 1967.

[28] Y. Bengio, "Learning deep architectures for AI," *Found. Trends Mach. Learn.*, vol. 2, no. 1, pp. 1–127, 2009.

[29] L. Bottou and O. Bousquet, "The tradeoffs of large scale learning," in *Proc. Adv. Neural Inf. Process. Syst.*, 2007, pp. 161–168.

[30] X. Glorot, A. Bordes, and Y. Bengio, "Deep sparse rectifier neural networks," in *Proc. 14th Int. Conf. Artif. Intell. Statist.*, 2011, pp. 315–323.

[31] V. Nair and G. E. Hinton, "Rectified linear units improve restricted Boltzmann machines," in *Proc. 27th Int. Conf. Mach. Learn. (ICML)*, Jun. 2010, pp. 807–814.

[32] R. Kohavi, "A study of cross-validation and bootstrap for accuracy estimation and model selection," in *Proc. 14th Int. Joint Conf. Artif. Intell.*, 1995, pp. 1137–1143.

[33] G. Lavenuta. Negative Temperature Coefficient Thermistors. QTI Sensing Solutions. Accessed: May 14, 2018. [Online]. Available: https://www.thermistor.com/sites/default/files/specsheets/Negative-Temperature-Coefficient-Thermistors.pdf

[34] V. S. Reinhardt, Y. C. Shih, P. A. Toth, S. C. Reynolds, and A. L. Berman, "Methods for measuring the power linearity of microwave detectors for radiometric applications," *IEEE Trans. Microw. Theory Techn.*, vol. 43, no. 4, pp. 715–720, Apr. 1995.

[35] C. S. Ruf, "Detection of calibration drifts in spaceborne microwave radiometers using a vicarious cold reference," *IEEE Trans. Geosci. Remote Sens.*, vol. 38, no. 1, pp. 44–52, Jan. 2000.

[36] C. Kummerow *et al.*, "The status of the tropical rainfall measuring mission (TRMM) after two years in orbit," *J. Appl. Meteorol.*, vol. 39, no. 12, pp. 1965–1982, Dec. 2000.

[37] M. Ablain, S. Philipps, N. Picot, and E. Bronner, "Jason-2 global statistical assessment and cross-calibration with Jason-1," *Mar. Geodesy*, vol. 33, pp. 162–185, Aug. 2010.

Mehmet Ogut received the B.S. degree in electrical and electronics engineering from Bogazici University, Istanbul, Turkey, in 2011, the M.S degree in electrical engineering from the George Washington University, Washington, DC, USA, in 2013, and the Ph.D. degree in electrical engineering from Colorado State University (CSU), Fort Collins, CO, USA, in 2018.

During his Ph.D. study, he focused on the Tropospheric Water and Cloud Ice (TWICE) small satellite instrument at the Microwave Systems Laboratory, CSU, as a Graduate Research Assistant. He focused on the design and testing command and data handling, power regulation boards, and on-orbit reliability analysis of the TWICE instrument including radiation testing and analysis of electrical components, and testing, characterization, and calibration of TWICE receivers. In addition, he focused on the deep-learning techniques on the microwave and millimeter-wave radiometry, and developing retrieval techniques for atmospheric water vapor from microwave and millimeter-wave radiometric measurements. He is currently a Post-Doctoral Research Fellow with the Microwave Instrument Science Group, Jet Propulsion Laboratory, California Institute of Technology, Pasadena, CA, USA. His expertise is design, testing, calibration, and analysis of microwave and millimeter-wave radiometer instruments.

Dr. Ogut is a member of Eta Kappa Nu, IEEE GRSS, and MTTS societies. He was the IEEE R5 ExCom Member from 2018 to 2019 and the Chair of the IEEE High Plains Section Young Professionals Affinity Group from 2017 to 2018.

Xavier Bosch-Lluis received the B.S and M.S degrees in telecommunications engineering from Universitat Politecnica de Catalunya (UPC), Barcelona, Spain, and the Ph.D. degree in remote sensing from the Department of Signal Theory and Communications, UPC.

He did a post-doc at the Microwave Systems Laboratory (MSL), Electrical and Computer Engineering Department, Colorado State University, Fort Collins, CO, USA. At MSL, he focused on the High-Frequency Airborne Microwave and Millimeter-wave Radiometer instrument to demonstrate increased spatial resolution of wet-tropospheric path delay retrieval for high-resolution ocean surface altimeter missions. He also focused on the Tropospheric Water and Could Ice (TWICE) instrument, designed for operation in a 6U CubeSat, with the scientific goal of providing global measurements of upper tropospheric water vapor as well as cloud ice particle size distribution and total cloud ice water content variability. He is currently a Technologist with the Microwave Systems Technology Group, Jet Propulsion Laboratory, California Institute of Technology, Pasadena, CA, USA. His expertise is in microwave and millimeter-wave radiometer design and calibration, as well as innovative digital radiometric concepts such as digital beamforming or polarization synthesis.

Steven C. Reising (S'88–M'98–SM'04) received the B.S.E.E. (*magna cum laude*) and M.S.E.E. degrees in electrical engineering from Washington University in St. Louis, St. Louis, MO, USA, and the Ph.D. degree in electrical engineering from Stanford University, Stanford, CA, USA, in 1998.

He was an Assistant Professor of electrical and computer engineering with the University of Massachusetts Amherst, Amherst, MA, USA, from 1998 to 2004, where he received tenure. He was a Summer Faculty Fellow with the Remote Sensing Division, Naval Research Laboratory, Washington, DC, USA, for three years. He has been a Full Professor of electrical and computer engineering with Colorado State University (CSU), Fort Collins, CO, USA, since 2011, where he served as an Associate Professor from 2004 to 2011. For the first six months of 2014, he was a Visiting Faculty Member with Sorbonne Universities, University of Paris VI, Paris, France, and Université Pierre et Marie Curie, Paris. His research interests include a broad range of remote sensing disciplines, including microwave remote sensing of the earth's atmosphere and oceans, earth science measurements from CubeSats and small satellites, radiometer systems from microwave to sub-millimeter-wave and terahertz frequencies (18–880 GHz), low-noise monolithic microwave integrated circuit design and packaging, lidar systems for sensing temperature and winds in the middle and upper atmosphere, lighting–ionosphere interactions, and atmospheric electrodynamics.

Dr. Reising is a member of URSI Commissions F, G, and H, the American Meteorological Society, the American Geophysical Union, the American Association for the Advancement of Science, Tau Beta Pi, and Eta Kappa Nu. He received the URSI Young Scientist Award at the General Assembly in Toronto, Canada, in 1999, the 2015 George T. Abell Outstanding Research Faculty Award from the College of Engineering at Colorado State University, the 2016 Outstanding Service Award from the U.S. National Committee of the International Union of Radio Science, presented at the Plenary Session of the 2016 National Radio Science Meeting in Boulder, CO, USA, the NSF CAREER Award from 2003 to 2008 in the areas of physical and mesoscale dynamic meteorology, the Office of Naval Research Young Investigator Program Award from 2000 to 2003 for passive microwave remote sensing of the oceans. His Ph.D. student S. Padmanabhan received the Second Prize Student Paper Award at IGARSS 2003 in Toulouse, France, as well as the URSI Young Scientist Award at the General Assembly in New Delhi, India, in 2005. While at Stanford, he received First Place in the USNC-URSI Student Paper Competition at the 1998 National Radio Science Meeting in Boulder, CO, USA. He has been the Principal Investigator of 14 grants from NASA, National Science Foundation, Department of Defense, Office of Naval Research, Naval Research Laboratory, National Polar-orbiting Operational Environmental Satellite System Integrated Program Office, European Space Agency, and Ball Aerospace and Technologies Corporation. He has served as a Principal Faculty Advisor for 16 M.S./Ph.D. students who have completed their degrees during the past 16 years and are now employed in universities, industry and government laboratories in the U.S., Europe, and Asia. He has been an elected Administrative Committee Member of the IEEE Geoscience and Remote Sensing Society (GRSS) since 2003 and serves as the Chair of the *Ad hoc* Committee for Intersocietal Relations. He has been an elected AdCom Member of the IEEE Microwave Theory and Techniques Society since 2004 and serves as the Vice Chair of operations. He served as the IEEE MTT-S Inter-Society Committee Chair from 2015 to 2018, the IEEE GRSS Vice President of Information Resources from 2011 to 2018, the IEEE GRSS as the Vice President of Technical Activities from 2008 to 2010, the Editor of the GRSS Newsletter from 2000 to 2002 and an Associate Editor for University Profiles from 1998 to 2000. He was a Founding Member of the Editorial Board of the IEEE GEOSCIENCE AND REMOTE SENSING LETTERS, with an impact factor of 1.8 in 2013, and served as an Associate Editor from 2004 to 2013. He has been a Guest Editor of four Special Issues of the IEEE TRANSACTIONS ON GEOSCIENCE AND REMOTE SENSING, with an impact factor of 4.7 in 2017. He served the U.S. National Committee of the International Union of Radio Science (USNC-URSI) as an Immediate Past Chair from 2015 to 2017, the Chair from 2012 to 2014, and the Secretary from 2009 to 2011 of all ten URSI Commissions (ten scientific and technical areas). He served as a Secretary of USNC-URSI Commission F (Wave Propagation and Remote Sensing) from 2004 to 2007. He chaired the USNC-URSI Student Paper Prize Competition from 2004 to 2008 and at the URSI North American Radio Science Meeting in Ottawa in 2007. He founded and chaired the first three URSI International Student Paper Prize Competitions at the URSI General Assemblies and Scientific Symposia held in Chicago, IL, USA, in 2008; Istanbul, Turkey, in 2011; and Beijing, China, in 2014. He served as a Technical Program Co-Chair for the USNC-URSI National Radio Science Meetings held each January in Boulder, CO, USA, from 2010 to 2014.